Piezoelectric Nanogenerators Based on Zinc Oxide Nanowire Arrays

Zhong Lin Wang[1,2,3]* and Jinhui Song[1]

We have converted nanoscale mechanical energy into electrical energy by means of piezoelectric zinc oxide nanowire (NW) arrays. The aligned NWs are deflected with a conductive atomic force microscope tip in contact mode. The coupling of piezoelectric and semiconducting properties in zinc oxide creates a strain field and charge separation across the NW as a result of its bending. The rectifying characteristic of the Schottky barrier formed between the metal tip and the NW leads to electrical current generation. The efficiency of the NW-based piezoelectric power generator is estimated to be 17 to 30%. This approach has the potential of converting mechanical, vibrational, and/or hydraulic energy into electricity for powering nanodevices.

Wireless devices may allow in situ, real-time biomedical monitoring and detection, but such devices still require a power source. Ideally, such devices should be self-powered and not dependent on a battery. The body provides numerous potential power sources: mechanical energy (such as body movement, muscle stretching, blood vessel contraction), vibrational energy (acoustic waves), chemical energy (glucose), and hydraulic energy (body fluid and blood flow), but the challenge is their efficient conversion into electrical energy. If accomplished on the nanoscale, such power sources could greatly reduce the size of integrated nanosystems for optoelectronics (*1*), biosensors (*2*), resonators (*3*), and more.

We demonstrate an approach to converting mechanical energy into electric power with the use of aligned zinc oxide (ZnO) nanowires (NWs). The mechanism of the power generator relies on the coupling of piezoelectric and semiconducting properties of ZnO as well as the formation of a Schottky barrier between the metal and ZnO contacts. The nanogenerator has the potential of harvesting energy from the environment for self-powered nanotechnology.

Among the known one-dimensional (1D) nanomaterials, ZnO has three key advantages. First, it exhibits both semiconducting and piezoelectric (PZ) properties that can form the basis for electromechanically coupled sensors and transducers. Second, ZnO is relatively biosafe and biocompatible (*4*), and it can be used for biomedical applications with little toxicity. Finally, ZnO exhibits the most diverse and abundant configurations of nanostructures known so far, such as NWs (*5*), nanobelts (NBs) (*6*), nanosprings (*7*), nanorings (*8*), nanobows (*9*), and nanohelices (*10*). Although numerous studies have demonstrated novel nanodevices and applications based on NWs and NBs, little work has been done to address the power needs of these nanosystems.

Our study is based on aligned ZnO nanowires grown on *c* plane–oriented α-Al_2O_3 substrate, using Au particles as a catalyst, by the vapor-liquid-solid (VLS) process (*11*, *12*). An epitaxial relation between ZnO and α-Al_2O_3 allows a thin, continuous layer of ZnO to form at the substrate, which serves as a large electrode connecting the NWs with a metal electrode for transport measurement (Fig. 1A). The NW grows along the [0001] direction and has side surfaces of {01$\bar{1}$0} (Fig. 1B). Most of the Au particles at the tips of the NWs either evaporate during the growth or fall off during scanning by the atomic force microscope (AFM) tip (fig. S1). For most of the NWs, the growth front is free of Au particles or has a small hemispherical Au particle that covers only a fraction of the top (inset, Fig. 1B). For the purpose of our measurements, we have grown NW arrays that have relatively less density and shorter length (0.2 to 0.5 μm), so that the AFM tip can exclusively reach one NW without touching another.

The measurements were performed by AFM using a Si tip coated with Pt film, which has a cone angle of 70°. The rectangular cantilever had a calibrated normal spring constant of 0.76 N/m (Fig. 1C). In the AFM contact mode, a constant normal force of 5 nN was maintained between the tip and sample surface. The tip scanned over the top of the ZnO NW, and the tip's height was adjusted according to the surface morphology and local contacting force. The thermal vibration of the NWs at room temperature was negligible. For the electric contact at the bottom of the nanowires, silver paste was applied to connect the (large) ZnO film on the substrate surface with the measurement circuit. The output voltage across an outside load of

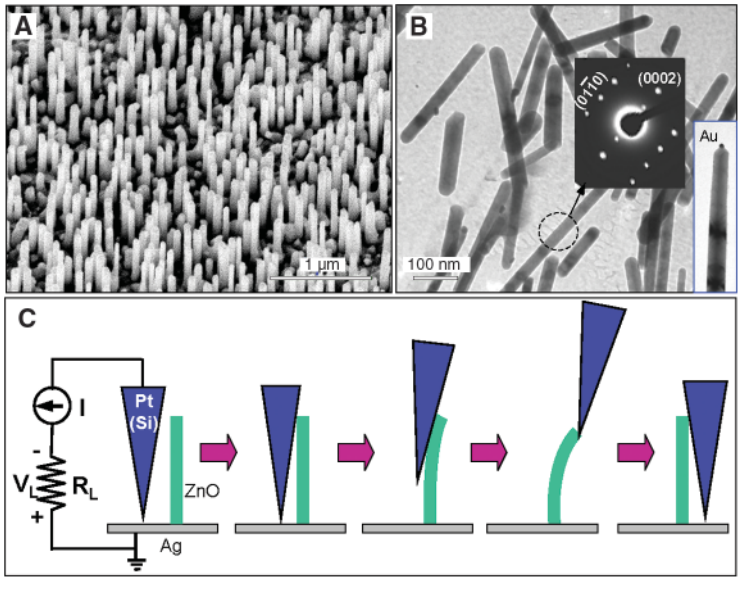

Fig. 1. Experimental design for converting nanoscale mechanical energy into electrical energy by a vertical piezoelectric (PZ) ZnO NW. (**A**) Scanning electron microscopy images of aligned ZnO NWs grown on α-Al_2O_3 substrate. (**B**) Transmission electron microscopy images of ZnO NWs, showing the typical structure of the NW without an Au particle or with a small Au particle at the top. Each NW is a single crystal and has uniform shape. Inset at center: an electron diffraction pattern from a NW. Most of the NWs had no Au particle at the top. Inset at right: image of a NW with an Au particle. (**C**) Experimental setup and procedures for generating electricity by deforming a PZ NW with a conductive AFM tip. The base of the NW is grounded and an external load of R_L is applied, which is much larger than the resistance R_i of the NW. The AFM scans across the NW arrays in contact mode.

[1]School of Materials Science and Engineering, Georgia Institute of Technology, Atlanta, GA 30332, USA. [2]Department of Advanced Materials and Nanotechnology, College of Engineering, Peking University, Beijing 100871, China. [3]National Center for Nanoscience and Technology, Beijing 100080, China.

*To whom correspondence should be addressed. E-mail: zhong.wang@mse.gatech.edu

resistance R_L = 500 megohms was continuously monitored as the tip scanned over the nanowires (note the defined polarity of the voltage signal). No external voltage was applied in any stage of the experiment.

Experimentally, both the topography (feedback signal from the scanner) (Fig. 2A) and the corresponding output voltage (V_L) images across the load (Fig. 2B) were recorded simultaneously when the AFM tip was scanned over the aligned NW arrays. In contact mode, as the tip scanned over the vertically aligned NWs, the NWs were bent consecutively. The bending distance was directly recorded in the topography image, from which the maximum bending deflection distance and the elastic modulus of the NW as well as the density of NWs that have been scanned by the tip were directly derived (*13*).

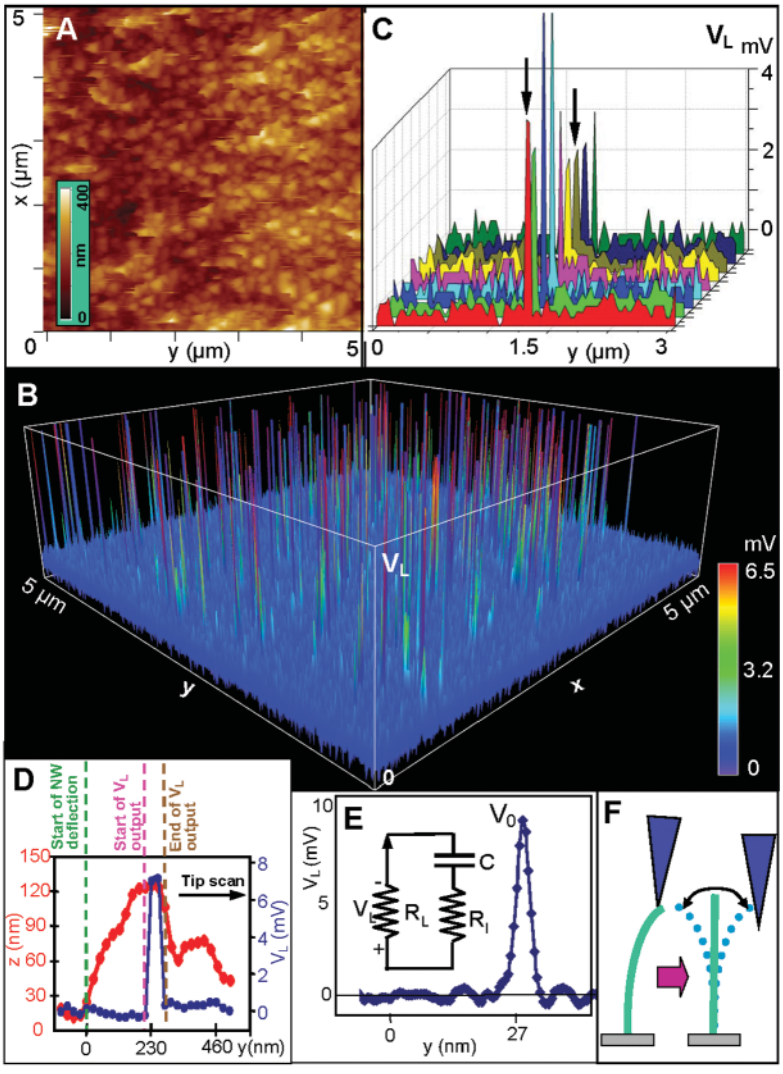

Fig. 2. Electromechanically coupled discharging process of aligned piezoelectric ZnO NWs observed in contact mode. (**A** and **B**) Topography image (A) and corresponding output voltage image (B) of the NW arrays. The discharging process was so rapid that each discharge event was characterized by only a couple of data points, which made it difficult to display the data by rainbow color (see fig. S2). (**C**) A series of line profiles of the voltage output signal when the AFM tip scanned across a vertical NW at a time interval of 1 min. The data show the registration of the electric signal with the location of the NW and the reproducibility of the event over an extended period of time. Colors represent the outputs required for a series of scans. In (A) to (C), the scanning speed of the tip was 12.081 μm/s, and the time spent to acquire and output one scan point was 2 ms. (**D**) Line profiles from the topography (red) and output voltage (blue) images across a NW. The peak of the voltage output corresponds approximately to the maximum deflection of the NW, indicating that the discharge occurs when the tip is in contact with the compressed side of the NW. When the tip touches the NW, PZ charges start to accumulate but no discharge occurs. Discharge occurs when the deflection reaches nearly the maximum y_m. Note that the lateral deflection y includes the shape and contact geometry of the tip, which must be subtracted to derive the true deflection of the NW. (**E**) Line profile of the voltage output signal when the AFM tip scans across a vertical NW at 12.394 μm/s. The time spent to acquire and output one scan point was 0.05 ms, which was achieved at the maximum scan frequency of the AFM. The inset is an equivalent circuit of the measurement to be used for simulating the discharging process. (**F**) The resonance vibration of a NW after being released by the AFM tip, showing that the stored elastic energy is transferred mainly into vibrational energy after creating the PZ discharge event.

In the V_L image, many sharp output peaks (like discharge peaks) were observed. These peaks, typically about 4 to 50 times the noise level, are rather sharp and narrow, and sometimes one or two pixels represent one voltage peak because of the limited scanning speed of the AFM tip, so that the color distribution in the plot is not easy to display (fig. S2). By reducing the scan range and increasing the scan frequency, more complete profiles of the discharge peaks were captured (fig. S3). Most of the voltage peaks are ~6 to 9 mV in height. The density of NWs contacted by the tip is counted from Fig. 2A to be ~20/μm^2, and the average density of NWs whose voltage output events had been captured by the tip in Fig. 2B is ~8/μm^2, thus ~40% of the NWs were contacted.

The location of the voltage peak is directly registered at the site of the NW. A time series of the voltage output line profiles across one NW acquired at a time interval of 1 min is shown in Fig. 2C. Because the dwell time for each data point (or pixel) is 2 ms, which is longer than the average lifetime of the voltage peak of ~0.6 ms (Fig. 2D), the peak at which V_L reached the maximum was possibly missed by the "slow" scanning tip, so that V_L shows a chopped top (arrows in Fig. 2C). A sharp peak can be identified continuously at the location of the NW and in the NW output voltage in each scan of the tip. When the tip started to deflect the NW, no voltage output was observed (Fig. 2D); V_L was detected when the deflection of the NW approached its maximum. When the NW was released by the AFM tip, V_L dropped to zero, indicating that the output of piezoelectricity was detected toward the end of the AFM scan over the NW.

The shape of the discharge peak can be further improved and analyzed by maximizing the tip scanning frequency and reducing the scanning range. Shown in Fig. 2E is a line profile of V_L when the tip was scanned over a single NW at a scanning velocity of 12.394 μm/s. The full width at half maximum (FWHM) of the voltage peak was estimated to be $\tau \sim 0.6$ ms. The damping behavior of the voltage peak can be qualitatively described with an equivalent circuit (*14*) (Fig. 2E). The NW is approximated as a resistor R_I and a capacitor C (including the contribution from the system). The lifetime of the output voltage V_L across the load R_L (note the polarity of the voltage) is $\tau = (R_L + R_I)C$ (*15*). For the experiment we have designed, the resistance of the NW R_I is negligible relative to R_L (*16*, *17*). Thus, the equivalent capacitance of the NW and the system is $C \approx \tau/R_L \approx 1.2$ pF.

The observed sharp voltage output for ZnO NWs was not observed for metal film (fig. S4), aligned carbon nanotubes (fig. S5), or aligned WO_3 NWs (fig. S6) under identical or similar experimental conditions. These data rule out the possibility of friction or contact potential as the source of the observed V_L response.

The efficiency of the electric power generated by this process can be calculated as follows. The output electrical energy from one NW in one piezoelectric discharge (PZD) event is $\Delta W_{PZD} = V_0^2C/2$ (*15*), where V_0 is the peak voltage of the discharge output. For simplicity, we approximately take the NW as a 2D object for easy analytical calculation. The elastic deformation energy (W_{ELD}) created by the AFM tip for displacing the NW is $W_{ELD} = 3YIy_m^2/2L^3$ (*15*), where Y is the elastic modulus, I is the moment of inertia, L is the length of the NW, and y_m is the maximum deflection of the NW. Dissipation of W_{ELD} mainly occurs in three ways: (i) mechanical resonance/vibration after releasing the NW (Fig. 2F); (ii) PZ discharge (ΔW_{PZD}) for each cycle of the vibration; and (iii) friction/viscosity from the environmental medium. The mechanical resonance of the NW continues for many cycles, but it is eventually damped by the viscosity of the medium. Each cycle of the vibration generates ΔW_{PZD}, but the AFM tip in the present experimental design catches only the energy generated in the first cycle of vibration. Taking into account the energy dissipated by the NW in the first cycle of vibration ΔW_{ELD} (*15*), the efficiency of converting mechanical energy to electrical energy is $\Delta W_{PZD}/\Delta W_{ELD}$. Therefore, an efficiency of 17 to 30% has been received for a cycle of the resonance (table S1). The large efficiency is likely due to the extremely large deformation that can be borne by the nanowire (*18*).

The physical principle for creating the PZ discharge energy arises from how the piezoelectric and semiconducting properties of ZnO are coupled. For a vertical, straight ZnO NW (Fig. 3A), the deflection of the NW by an AFM tip creates a strain field, with the outer surface being stretched (positive strain ε) and the inner surface compressed (negative ε) (Fig. 3B). An electric field E_z along the NW (z direction) is then created inside the NW volume through the PZ effect, $E_z = \varepsilon_z/d$, where d is the PZ coefficient (*19*) along the NW direction that is normally the positive c axis of ZnO, with the Zn atomic layer being the front-terminating layer (*20*, *21*). The PZ field direction is closely parallel to the z axis (NW direction) at the outer surface and antiparallel to the z axis at the inner surface (Fig. 3C). Under the first-order approximation, across the width of the NW at the top end, the electric potential distribution from the compressed to the stretched side surface is approximately between V_s^- to V_s^+ [with $V_s^\mu = \mu 3T|y_m|/4Ld$ (*15*), where T is the thickness of the NW). The electrode at the base of the NW is grounded. Note that V_s^+ and V_s^- are the voltages produced by the PZ effect, which are each typically larger than a few tens of volts (*22*). The potential is created by the relative displacement of the Zn^{2+} cations with respect to the O^{2-} anions, a result of the PZ effect in the wurtzite crystal structure; thus, these ionic charges cannot freely move and cannot recombine without releasing the strain (Fig. 3D). The potential difference is maintained as long as the deformation is in place and no foreign free charges (such as from the metal contacts) are injected.

The contacts at the top and the base of the NW are nonsymmetric; the bottom contact is to the ZnO film in contact with Ag paste, so the effective contact is between ZnO and Ag. The electron affinity (E_a) of ZnO is 4.5 eV (*23*) and the work function (ϕ) of Ag is 4.2 eV; there is no barrier at the interface, so the ZnO-Ag contact is ohmic. At the tip of the NW, Pt has ϕ = 6.1 eV, and the Pt-ZnO contact is a Schottky barrier (*24*, *25*) and dominates the entire transport process. Because the compressed side of the semiconductor ZnO NW has negative potential V_s^- and the stretched side has positive potential (V_s^+), two distinct transport processes will occur across the Schottky barrier.

We now consider the case of a ZnO NW without an Au particle at the top. In the first step, the AFM conductive tip that induces the deformation is in contact with the stretched surface of positive potential V_s^+ (Fig. 3, D and E). The Pt metal tip has a potential of nearly zero, $V_m = 0$, so the metal tip–ZnO interface is negatively biased for $\Delta V = V_m - V_s^+ < 0$. Because the as-synthesized ZnO NWs behave as n-type semiconductors, the Pt metal–ZnO semiconductor (M-S) interface in this case is a reverse-biased Schottky diode (Fig. 3E), and little current flows across the interface. In the second step, when the AFM tip is in contact with the compressed side of the NW (Fig. 3F), the metal tip–ZnO interface is positively biased for $\Delta V = V_L = V_m - V_s^- > 0$. The M-S interface in this

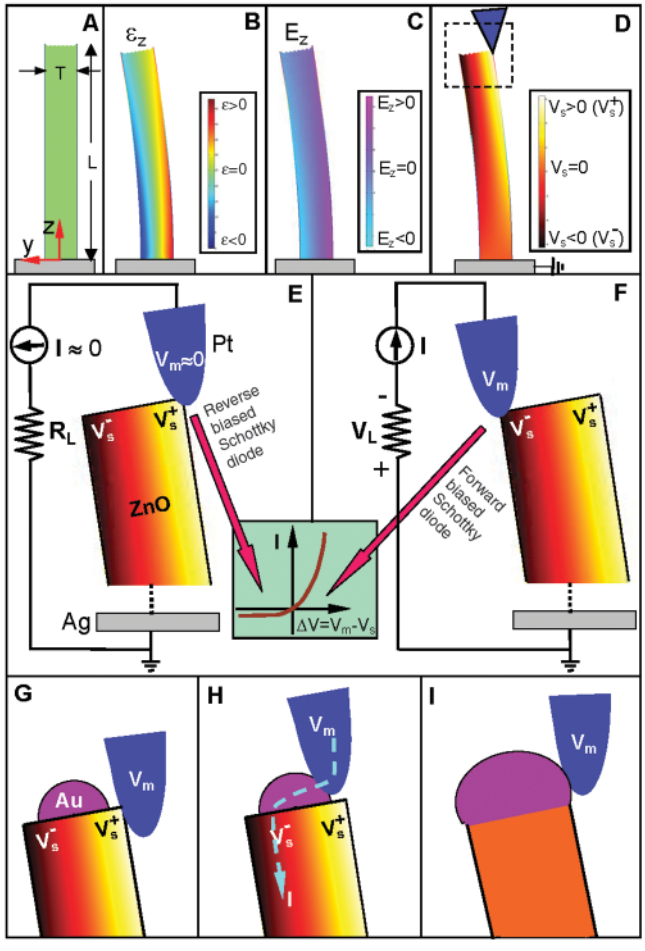

Fig. 3. Transport is governed by a metal-semiconductor Schottky barrier for the PZ ZnO NW (see movies S1 and S2). (**A**) Schematic definition of a NW and the coordination system. (**B**) Longitudinal strain ε_z distribution in the NW after being deflected by an AFM tip from the side. The data were simulated by FEMLAB for a ZnO NW of length 1 μm and an aspect ratio of 10. (**C**) The corresponding longitudinal PZ-induced electric field E_z distribution in the NW. (**D**) Potential distribution in the NW as a result of the PZ effect. (**E** and **F**) Contacts between the AFM tip and the semiconductor ZnO NW [boxed area in (D)] at two reversed local contact potentials (positive and negative), showing reverse- and forward-biased Schottky rectifying behavior, respectively (see text). This oppositely biased Schottky barrier across the NW preserves the PZ charges and later produces the discharge output. The inset shows a typical current-voltage (*I-V*) relation characteristic of a metal-semiconductor (n-type) Schottky barrier. The process in (E) is to separate and maintain the charges as well as build up the potential. The process in (F) is to discharge the potential and generates electric current. (**G** and **H**) Contact of the metal tip with a ZnO NW with a small Au particle at the top. The PZ potential is built up in the displacing process (G), and later the charges are released through the compressed side of the NW (H). (**I**) Contact of the metal tip with a ZnO NW with a large Au particle at the top. The charges are gradually "leaked" out through the compressed side of the NW as soon as the deformation occurs; thus, no accumulated potential will be created.

case is a positively biased Schottky diode, and it produces a sudden increase in the output electric current. The current is the result of ΔV-driven flow of electrons from the semiconductor ZnO NW to the metal tip. The flow of the free electrons from the loop through the NW to the tip will neutralize the ionic charges distributed in the volume of the NW and thus will reduce the magnitudes of the potential V_s^- and V_s^+. Thus, V_L starts to drop and reaches zero after all of the ionic charges in the NW are fully neutralized. This mechanism explains why the discharge curve in Fig. 2E is nearly symmetric. According to the model, the discharge occurs when the NW is bent nearly to its maximum deflection, so V_L should have a small offset in reference to the corresponding topography peak along the direction of tip scan, as is observed experimentally in Fig. 2D.

We next consider the case of a ZnO NW with a small Au particle at the top as a result of VLS growth (Fig. 3, G and H). In the first step of the AFM tip displacing the NW, the tip is directly in contact with the ZnO NW but not the Au particle (Fig. 3G) because of its small size and hemispherical shape (Fig. 1B and fig. S1). A process similar to that described in Fig. 3E occurs, and no output voltage will be observed. When the tip is in contact with the Au particle, the tip is integrated with the particle as one metal contact, and at the local interface between the Au particle and the negatively charged, compressed side of the ZnO NW (V_s^-), a forward-biased Schottky diode is formed; thus, the current flows from the tip through the Au particle to the interface region with negative PZ voltage (V_s^-) (Fig. 3H). A discharge process similar to that shown in Fig. 3F occurs, and a sharp voltage output is produced.

In the case of a NW with a large Au particle that fully covers its top (Fig. 3I), the metal tip is directly in touch with the Au tip at the beginning of the forced displacement. Because of the conducting channel at the compressed side of the NW, the polar charges produced by the displaced Zn^{2+} and O^{2-} ions caused by the PZ effect are immediately neutralized by external free charges as soon as they are produced by the deformation. Therefore, no accumulative potential profile is formed at the M-S interface, and no measurable output voltage is detected in the experimental setup we have designed (Fig. 1C).

We also measured the PZ voltage output for the same samples of aligned ZnO NWs in the AFM tapping mode. In this case, the deformation occurred longitudinally and there was no side displacement. The NW was vertically compressed, so the voltage created at the top of the NW was negative V_s^- so long as the base electrode was grounded (Fig. 4A). There was no voltage drop across the width of the NW. Thus, across the metal tip–ZnO interface, a positively biased Schottky diode formed and the electrons could freely flow across the interface. Electrons flowed as the deformation occurred, and there was no accumulation of net charge in the NW volume. This type of slowly "leaked" current produces no detectable signal. Therefore, for the ZnO NWs whose AFM image in tapping mode is shown in Fig. 4B, no output voltage V_L was detected beyond the noise level (Fig. 4C).

We now estimate the possibility of powering nanodevices with the NW-based power generator. From table S1, the PZ energy output by one NW in one discharge event is ~0.05 fJ, and the output voltage on the load is ~8 mV. For a NW of typical resonance frequency ~10 MHz, the output power of the NW would be ~0.5 pW. If the density of NWs per unit area on the substrate is 20/μm², the output power density is ~10 pW/μm². By choosing a NW array of size 10 μm × 10 μm, the power generated may be enough to drive a single NW/NB/nanotube-based device (*26*–*28*). If we can find a way to induce the resonance of a NW array and output the PZ-converted power generated in each cycle of the vibration, a significantly strong power source may be possible for self-powering nanodevices. Furthermore, if the energy produced by acoustic waves, ultrasonic waves, or hydraulic pressure/force could be harvested, electricity could be generated by means of ZnO NW arrays grown on solid substrates or even on flexible polymer films (*29*). The principle and the nanogenerator demonstrated could be the basis for new self-powering nanotechnology that harvests electricity from the environment for applications such as implantable biomedical devices, wireless sensors, and portable electronics (*29*).

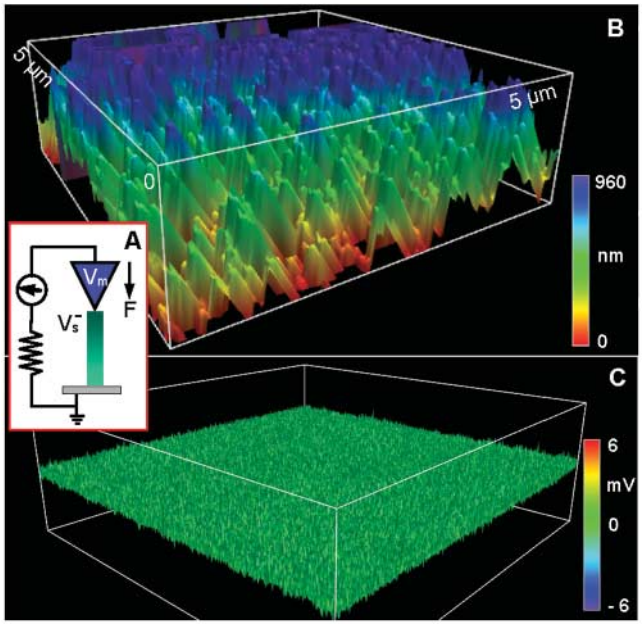

Fig. 4. Electromechanically coupled discharging process of aligned piezoelectric ZnO NWs observed in tapping mode. (**A**) Experimental setup. (**B** and **C**) Topography image (B) and corresponding output voltage image (C) of the NWs. The tapping force was 5 nN, tapping frequency 68 KHz, and tapping speed 6 μm/s. The voltage output contains no information but noise, proving the physical mechanism demonstrated in Fig. 3.

References and Notes

1. X. F. Duan, Y. Huang, R. Agarwal, C. M. Lieber, *Nature* **421**, 241 (2003).
2. G. F. Zheng, F. Patolsky, Y. Cui, W. U. Wang, C. M. Lieber, *Nat. Biotechnol.* **23**, 1294 (2005).
3. X. D. Bai, P. X. Gao, Z. L. Wang, E. G. Wang, *Appl. Phys. Lett.* **82**, 4806 (2003).
4. J. Zhou, N. S. Xu, Z. L. Wang, unpublished data.
5. M. H. Huang *et al.*, *Adv. Mater.* **13**, 113 (2001).
6. Z. W. Pan, Z. R. Dai, Z. L. Wang, *Science* **291**, 1947 (2001).
7. X. Y. Kong, Z. L. Wang, *Nano Lett.* **3**, 1625 (2003).
8. X. Y. Kong, Y. Ding, R. Yang, Z. L. Wang, *Science* **303**, 1348 (2004).
9. W. L. Hughes, Z. L. Wang, *J. Am. Chem. Soc.* **126**, 6703 (2004).
10. P. X. Gao *et al.*, *Science* **309**, 1700 (2005).
11. X. D. Wang, C. J. Summers, Z. L. Wang, *Nano Lett.* **3**, 423 (2004).
12. X. D. Wang *et al.*, *J. Am. Chem. Soc.* **127**, 7920 (2005).
13. J. H. Song, X. D. Wang, E. Riedo, Z. L. Wang, *Nano Lett.* **5**, 1954 (2005).
14. A piezoelectric material can be approximately characterized by a capacitor and a resistor. The capacitor represents the piezoelectric charges accumulated in the volume, and the resistor represents its inner resistance.
15. See supporting material on *Science* Online.
16. From our recent measurements of ZnO nanowires, the resistivity is from 10^{-2} to 10 ohm·cm (*17*) depending on the contacts at the electrodes and the concentration of oxygen vacancies. For a NW of length 0.2 μm and diameter 40 nm, the resistance is between 16 kilohms and 16 megohms, which is much smaller than the applied external load of 500 megohms. Here we ignored the resistance produced by the ZnO film at the bottom of the nanowires because it is very large and covers the entire area of the substrate; thus, the inner resistance is dominated by the NW.
17. J. H. He, C. S. Lao, L. J. Chen, D. Davidovic, Z. L. Wang, *J. Am. Chem. Soc.* **127**, 16376 (2005).
18. W. L. Hughes, Z. L. Wang, *Appl. Phys. Lett.* **86**, 043106 (2005).
19. M. H. Zhao, Z. L. Wang, S. X. Mao, *Nano Lett.* **4**, 587 (2004).
20. The wurtzite-structured ZnO can be described as a number of alternating planes composed of tetrahedrally coordinated O^{2-} and Zn^{2+} ions stacked alternatively along the *c* axis. The oppositely charged ions produce positively charged (0001)-Zn and negatively charged $(000\bar{1})$-O polar surfaces. The Zn-terminated surface is at the growth front (positive *c*-axis direction) because of its higher catalytic activity (*19*).
21. Z. L. Wang, X. Y. Kong, J. M. Zuo, *Phys. Rev. Lett.* **91**, 185502 (2003).

22. A simple calculation indicates that the magnitudes of V_s^+ and V_s^- are on the order of a few tens to hundreds of volts. In practice, if we consider the polarization and dielectric screening in the calculation, the local potential is much smaller than the numbers given by the equations here. An accurate calculation of the potential distribution as a result of the ionic charges introduced by the PZ effect and the surface charges caused by boundaries must be solved numerically and self-consistently. In our analysis, a correct magnitude and sign of the potential is sufficient for illustrating the physical model.
23. S. Hasegawa, S. Nishida, T. Yamashita, H. Asahi, *J. Ceramic Proc. Res.* **6**, 245 (2005).
24. R. F. Pierret, *Semiconductor Device Fundamentals* (Addison-Wesley, Reading, MA, 1996), chapter 14.
25. W. I. Park, G. C. Yi, J. W. Kim, S. M. Park, *Appl. Phys. Lett.* **82**, 4358 (2003).
26. Y. Huang *et al.*, *Science* **294**, 1313 (2001).
27. A. Bachtold, P. Hadley, T. Nakanishi, C. Dekker, *Science* **294**, 1317 (2001); published online 4 October 2001 (10.1126/science.1065824).
28. J. Chen *et al.*, *Science* **310**, 1171 (2005).
29. U.S. patent pending.
30. Supported by NSF grant DMR 9733160, the NASA Vehicle Systems Program and Department of Defense Research and Engineering, and the Defense Advanced Research Projects Agency. We thank X. Wang, W. L. Hughes, J. Zhou, and J. Liu for their help.

Supporting Online Material
www.sciencemag.org/cgi/content/full/312/5771/242/DC1
SOM Text
Figs. S1 to S6
Table S1
Movies S1 and S2

19 December 2005; accepted 10 March 2006
10.1126/science.1124005

Control of Electron Localization in Molecular Dissociation

M. F. Kling,[1] Ch. Siedschlag,[1] A. J. Verhoef,[2] J. I. Khan,[1] M. Schultze,[2] Th. Uphues,[3] Y. Ni,[1] M. Uiberacker,[4] M. Drescher,[3,5] F. Krausz,[2,4] M. J. J. Vrakking[1]

We demonstrated how the subcycle evolution of the electric field of light can be used to control the motion of bound electrons. Results are presented for the dissociative ionization of deuterium molecules ($D_2 \rightarrow D^+ + D$), where asymmetric ejection of the ionic fragment reveals that light-driven intramolecular electronic motion before dissociation localizes the electron on one of the two D^+ ions in a controlled way. The results extend subfemtosecond electron control to molecules and provide evidence of its usefulness in controlling reaction dynamics.

Few-cycle laser light with a controlled evolution of the electric field $E(t) = a(t) \times \cos(\omega t + \varphi)$, with amplitude $a(t)$, frequency ω, and carrier envelope phase φ (*1*), has recently allowed the steering of the motion of electrons in and around atoms on a subfemtosecond time scale. Manifestations of this control include the reproducible generation and measurement of single subfemtosecond pulses (*2*, *3*) and controlled electron emission from atoms (*4*, *5*). Here we address the question of whether this control can be extended to electron wave packets in molecules and, if so, can light-field–driven electronic motion affect reaction dynamics?

Many of the processes in terms of which strong-field molecular interactions are presently interpreted (such as bond softening and enhanced ionization) were discovered in experimental and theoretical work on H_2 and its isotopes HD and D_2 [see (*6*) and references therein]. The role of phase control in the dissociation of hydrogen has recently been addressed in a few theoretical studies (*7*–*9*). We present experiments on the dissociation of D_2^+ into $D^+ + D$ by intense few-cycle laser pulses with controlled field evolution and report a pronounced dependence of the direction of the D^+ ejection (and hence of the localization of the electron in the system) on the waveform driving the reaction. Quantum-classical computations reveal that light-field control of molecular electron dynamics is responsible for the observed phenomenon.

The dynamics of molecules in intense laser fields typically includes ionization and dissociation. The dissociation of D_2 in intense laser fields is known to involve several pathways whose relative importance depends on intensity and pulse duration (*6*). The formation of fragment ions occurs via a two-step mechanism (Fig. 1A) in which initially the molecule is ionized by the laser field (Fig. 1A, red arrow) and a vibrational wave packet is launched in the $1s\sigma_g^+$ state. Breakup of the D_2^+ ion is triggered by excitation to a repulsive state or after double ionization.

In the single-ionization pathways, excitation of bound D_2^+ (such as to the $2p\sigma_u^+$ state in Fig. 1A) by recollision of the first electron [recollision excitation (RCE), green line] or directly by the laser field [sequential excitation (SE), blue line] leads to dissociation and the formation of a D^+ ion and a D atom. For example, in recent molecular clock studies, vibrational motion in D_2^+ was time-resolved by exploiting RCE (*10*, *11*). Additional dissociation mechanisms can be understood by considering that molecular potentials are modified by strong laser fields. Bond softening (BS, purple line) (*12*) occurs when energy gaps open up at avoided crossings between adiabatic field-dressed potential energy curves.

In double-ionization pathways, the formation of D_2^+ is followed by a second ionization

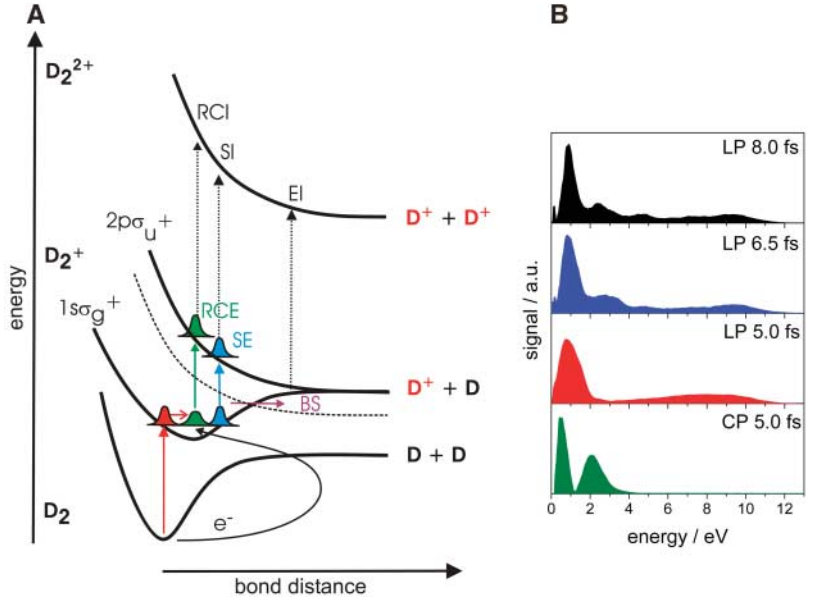

Fig. 1. (**A**) Pathways for the production of D^+ ions from D_2 by dissociation of the molecular ion (through BS, SE, or RCE) or by Coulomb explosion (through RCI, SI, or EI). BS occurs when the avoided crossing between diabatic potentials that are dressed by the laser field gives rise to dissociation from vibrational levels that were originally bound (*12*). (**B**) D^+ kinetic energy spectra for dissociation of D_2 by 5- to 8-fs linearly polarized (LP) and 5-fs circularly polarized (CP) laser pulses without phase stabilization, at $I = 1.2 \pm 0.2 \times 10^{14}$ W cm^{-2} and $I = 2.4 \pm 0.2 \times 10^{14}$ W cm^{-2}, respectively.

[1]FOM Instituut voor Atoom en Molecuul Fysica (AMOLF), Kruislaan 407, 1098 SJ Amsterdam, Netherlands. [2]Max-Planck-Institut für Quantenoptik, Hans-Kopfermann-Strasse 1, D-85748 Garching, Germany. [3]Fakultät für Physik, Universität Bielefeld, Universitätsstrasse 25, D-33615 Bielefeld, Germany. [4]Department für Physik, Ludwig-Maximilians-Universität München, Am Coulombwall 1, D-85748 Garching, Germany. [5]Institut für Experimentalphysik, Universität Hamburg, Luruper Chaussee 149, D-22761 Hamburg, Germany.